

Simulations of partially coherent focal plane imaging arrays: Fisher matrix approach to performance evaluation

G. Saklatvala,^{*} S. Withington,[†] and M. Hobson[‡]

Cavendish Laboratory, J.J. Thomson Avenue, Cambridge CB3 0HE, UK

Submitted to MNRAS 7 March 2007

ABSTRACT

Focal plane arrays of bolometers are increasingly employed in astronomy at far-infrared to millimetre wavelengths. The focal plane fields and the detectors are both partially coherent in these systems, but no account has previously been taken of the effect of partial coherence on array performance. In this paper, we use our recently developed coupled-mode theory of detection together with Fisher information matrix techniques from signal processing to characterize the behaviour of partially coherent imaging arrays. We investigate the effects of the size and coherence length of both the source and the detectors, and the packing density of the array, on the amount of information that can be extracted from observations with such arrays.

Key words: instrumentation: detectors, methods: numerical, methods: statistical, techniques: image processing, infrared, submillimetre

1 INTRODUCTION

Large format focal plane imaging arrays are of increasing importance in many areas of submillimetre wave astronomy. Arrays utilising semiconducting bolometers have already been built for the Stratospheric Observatory For Infrared Astronomy (SOFIA) (Evans et al. 2002) and SHARC II (Dowell et al. 2003), each of which utilises 12×32 arrays. Future arrays are planned using transition edge sensors, including SCUBA 2 (Holland et al. 2006), GISMO (Staguhn et al. 2006) and arrays for the Green Bank Telescope (GBT) (Dicker et al. 2006), Atacama Cosmology Telescope (ACT) (Fowler 2004) and CLOVER (Maffei et al. 2005). The largest of these planned arrays is of size 64×64 pixels.

The construction of imaging arrays such as these, all of which operate at wavelengths between 0.05mm and 3mm, presents difficulties in understanding their behaviour. Crucially, no account has previously been taken of the effects of coherence on the performance of an array. This is important for two reasons. Firstly, at the wavelengths concerned telescopes are few moded, resulting in a partially coherent field in the focal plane, with correlations between different pixels. Secondly, the detectors used in the arrays are only a few wavelengths in size (in the case of ACT less than a wavelength), and should be expected therefore to show partially coherent behaviour themselves. If partially coherent imaging arrays are to be used successfully for astronomical observations, it is essential to understand their behaviour.

In the past, understanding of partially coherent detectors was limited by the lack of practical modelling techniques. In a recent paper (Saklatvala, Withington & Hobson 2007) we developed a general theory of partially coherent detection; in this paper we apply the technique to the simulation of imaging arrays. Qualitatively, coherence has two effects: it increases the noise associated with the statistical variation of the incoming field, and leads to correlations in this noise. We employ a Fisher matrix analysis to gain insight into how these effects alter array performance. In our simulations, we compare the ability of different arrays to recover information about some simple sources. Specifically, we focus on the size and coherence both of the detectors and the sources, and the packing density of the array. We anticipate that such analyses will prove useful in the design of the next generation of astronomical focal plane bolometric imaging arrays.

^{*} Email: g.saklatvala@mrao/cam.ac.uk

[†] Email: stafford@mrao.cam.ac.uk

[‡] Email: mph@mrao.cam.ac.uk

2 THEORY OF PARTIALLY COHERENT DETECTORS

In earlier papers (Withington & Yassin 2001, 2002; Saklatvala, Withington & Hobson 2007) we derived the following expression for the average power absorbed by a paraxial multimode power detector from a statistically stationary source:

$$\langle P \rangle = \int_0^\infty d\omega \sum_{i=1}^2 \sum_{j=1}^2 \int_{\mathcal{S}} d\mathbf{r}_1 \int_{\mathcal{S}} d\mathbf{r}_2 Z_{ij}^*(\mathbf{r}_1, \mathbf{r}_2, \omega) Y_{ij}(\mathbf{r}_1, \mathbf{r}_2, \omega), \quad (1)$$

where $Y_{ij}(\mathbf{r}_1, \mathbf{r}_2, \omega)$ is the cross-spectral density

$$Y_{ij}(\mathbf{r}_1, \mathbf{r}_2, \omega) = \int_{-\infty}^\infty e^{-i\omega u} \langle E_i(\mathbf{r}_1, t) E_j^*(\mathbf{r}_2, t + u) \rangle du, \quad (2)$$

and $E_i(\mathbf{r}_1, t)$ is the i th component of the analytic signal associated with the incoming electric field at position \mathbf{r}_1 and time t . \mathcal{S} is a surface normal to the wavevector characterizing the input of the detector, and the sums are over the two polarizations normal to the wavevector. $Z_{ij}(\mathbf{r}_1, \mathbf{r}_2, \omega)$ is a quantity characterizing the detector which we call the ‘detector coherence tensor’. We have derived (1) in several ways, using thermodynamic arguments (Withington & Yassin 2001), reciprocity (Withington & Yassin 2002), and general arguments about the properties of detectors (Saklatvala et al. 2007). The result is effectively a weighted linear sum of all pairs of space–time correlations in the incoming field, and may be interpreted also in terms of the coupling between the natural modes of the incoming field and a set of modes that characterizes the detector. The power of our theory is that, in addition to calculating the average detector outputs, it also allows us to relate the statistics of the incoming fields to the statistics of the detector outputs. For a thermal source, for an integration time much longer than either the coherence time of the source or the response time of the detector, the covariance of the power recorded by two detectors is

$$\begin{aligned} \text{Cov}[P^a, P^b] &= \frac{1}{\tau} \int_0^\infty d\omega \sum_{i=1}^2 \sum_{j=1}^2 \sum_{k=1}^2 \sum_{l=1}^2 \int_{\mathcal{S}} d\mathbf{r}_1 \int_{\mathcal{S}} d\mathbf{r}_2 \int_{\mathcal{S}} d\mathbf{r}_3 \int_{\mathcal{S}} d\mathbf{r}_4 Z_{ji}^{a*}(\mathbf{r}_2, \mathbf{r}_1, \omega) Y_{jk}(\mathbf{r}_2, \mathbf{r}_3, \omega) Z_{lk}^{b*}(\mathbf{r}_4, \mathbf{r}_3, \omega) Y_{li}(\mathbf{r}_4, \mathbf{r}_1, \omega) \\ &\quad + \frac{\delta_{ab}}{\tau} \int_0^\infty d\omega \sum_{i=1}^2 \sum_{j=1}^2 \int_{\mathcal{S}} d\mathbf{r}_1 \int_{\mathcal{S}} d\mathbf{r}_2 \hbar \omega Z_{ij}^{a*}(\mathbf{r}_1, \mathbf{r}_2, \omega) Y_{ij}(\mathbf{r}_1, \mathbf{r}_2, \omega), \end{aligned} \quad (3)$$

where τ is the integration time. (3) can be derived using either a semi–classical (Saklatvala et al. 2007) or quantum optical (Zmuidzinas 2003; Withington, Hobson & Saklatvala 2005) approach. (3) gives both the fluctuations of the detector outputs and the correlations between the outputs, and thus incorporates the Hanbury Brown–Twiss effect (Hanbury Brown & Twiss 1956).

In most applications, a frequency filter is placed in front of a detector to restrict the bandwidth (this is necessary to avoid blurring of the image, in the case of an array, or ambiguity in the baselines, in the case of an interferometer). As an idealization, we consider a filter that multiplies the cross–spectral density by a top hat function with central frequency ω_0 and bandwidth $\Delta\omega$. To avoid blurring, the bandwidth must be sufficiently small that the cross-spectral density and the detector coherence tensor are approximately constant across the bandwidth of the detector, in which case

$$\langle P \rangle \simeq \Delta\omega \sum_{i=1}^2 \sum_{j=1}^2 \int_{\mathcal{S}} d\mathbf{r}_1 \int_{\mathcal{S}} d\mathbf{r}_2 Z_{ij}^*(\mathbf{r}_1, \mathbf{r}_2, \omega_0) Y_{ij}(\mathbf{r}_1, \mathbf{r}_2, \omega_0), \quad (4)$$

and

$$\begin{aligned} \text{Cov}[P^a, P^b] &\simeq \frac{\Delta\omega}{\tau} \sum_{i=1}^2 \sum_{j=1}^2 \sum_{k=1}^2 \sum_{l=1}^2 \int_{\mathcal{S}} d\mathbf{r}_1 \int_{\mathcal{S}} d\mathbf{r}_2 \int_{\mathcal{S}} d\mathbf{r}_3 \int_{\mathcal{S}} d\mathbf{r}_4 Z_{ji}^{a*}(\mathbf{r}_2, \mathbf{r}_1, \omega_0) Y_{jk}(\mathbf{r}_2, \mathbf{r}_3, \omega_0) Z_{lk}^{b*}(\mathbf{r}_4, \mathbf{r}_3, \omega_0) Y_{li}(\mathbf{r}_4, \mathbf{r}_1, \omega_0) \\ &\quad + \frac{\hbar\omega_0 \Delta\omega \delta_{ab}}{\tau} \sum_{i=1}^2 \sum_{j=1}^2 \int_{\mathcal{S}} d\mathbf{r}_1 \int_{\mathcal{S}} d\mathbf{r}_2 Z_{ij}^{a*}(\mathbf{r}_1, \mathbf{r}_2, \omega_0) Y_{ij}(\mathbf{r}_1, \mathbf{r}_2, \omega_0). \end{aligned} \quad (5)$$

For numerical work we must discretize the integrals in (4) and (5). The idealized detectors we simulate in this paper respond equally to all polarizations, so defining

$$Z_{\alpha\beta} = (\Delta x)^2 Z_{ij}(\mathbf{r}_\alpha, \mathbf{r}_\beta, \omega_0) \quad (6)$$

$$Y_{\alpha\beta} = \sum_{ij} Y_{ij}(\mathbf{r}_\alpha, \mathbf{r}_\beta, \omega_0) \quad (7)$$

for some regular grid of sample points $\{\mathbf{r}_\alpha\}$ with spacing Δx , we obtain

$$\langle P \rangle \sim \Delta\omega \text{Tr} \mathbf{Z} \mathbf{Y}, \quad (8)$$

and

$$\text{Cov}[P^a, P^b] \sim \frac{\Delta\omega}{\tau} \left(\text{Tr} \mathbf{Z}^a \mathbf{Y} \mathbf{Z}^b \mathbf{Y} + \delta^{ab} \hbar\omega_0 \text{Tr} \mathbf{Z}^a \mathbf{Y} \right). \quad (9)$$

Note that we have used italic letters to denote the continuous tensors and Roman letters to denote the discretized forms.

In the single mode case, the signal-to-noise ratio $P/\sqrt{\text{Cov}[P, P]}$ obtained from (8) and (9) reduces to the Dicke radiometer equation (Dicke 1946) in the high occupancy limit, and Poisson noise in the low occupancy limit. In this paper we are interested in the long wavelength, high occupancy limit, so we neglect the second term of (9).

3 PARAMETER ESTIMATION FROM IMAGING ARRAYS

A crucial factor in measuring the performance of an imaging array is the amount of information that can be extracted from it. To this end, we employ the technique of Fisher matrix analysis, which is widely used in many areas of astronomy (Tegmark, Taylor & Heavens 1997; Hamilton 1997; Yamamoto et al. 2001; Martins et al. 2002; Rocha et al. 2004), particularly the constraint of cosmological parameters from CMB measurements, and has also been applied to the design of radio interferometry arrays (Stoica & Nehorai 1989; Abramovich et al. 1996; Adorf 1996), but has not hitherto to our knowledge been employed in the context of focal plane imaging arrays. The Fisher matrix analysis technique provides a way of estimating the uncertainties and correlations in the parameters of a model fitted to some data, averaged over all realisations of the data, and without the need to enumerate specific realisations. In this paper we perform simulations to estimate the constraints on the parameters of a source when observed with imaging arrays of different size, coherence and packing density.

Given a data column vector \mathbf{D} and a model \mathcal{H} with parameter column vector $\boldsymbol{\theta}$, the Fisher information matrix is equal to minus the expected curvature of the logarithm of the likelihood:

$$F_{ij}[\boldsymbol{\theta}, \mathcal{H}] = -\text{E} \left[\frac{\partial^2}{\partial \theta_i \partial \theta_j} \ln \Pr(\mathbf{D}|\boldsymbol{\theta}, \mathcal{H}) \right]. \quad (10)$$

For a uniform prior, the posterior is proportional to the likelihood, so the Fisher matrix is also equal to minus the expected curvature of the logarithm of the posterior. Applying the Gaussian approximation to the posterior, we see that the covariance matrix of the recovered parameters can be estimated by inverting the Fisher matrix for the parameter values at the maximum of the posterior. Indeed it can be shown (Marzetta 1993, and see Appendices A and B) that the inverse of the Fisher matrix provides a lower bound for the covariance matrix of any unbiased estimators of the parameters (the Cramér–Rao bound).

The Fisher matrix at the maximum of the posterior can itself be estimated from the mean and covariance of the data, and the derivatives of these quantities with respect to the parameters. Applying the Gaussian approximation to the likelihood function, we can show (see Appendix C) that

$$F_{ij}[\boldsymbol{\theta}_0, \mathcal{H}] \simeq \frac{\partial \boldsymbol{\mu}^T[\boldsymbol{\theta}_0, \mathcal{H}]}{\partial \theta_i} \boldsymbol{\Sigma}^{-1}[\boldsymbol{\theta}_0] \frac{\partial \boldsymbol{\mu}[\boldsymbol{\theta}_0]}{\partial \theta_j} + \frac{1}{2} \text{Tr} \left(\boldsymbol{\Sigma}^{-1}[\boldsymbol{\theta}_0, \mathcal{H}] \frac{\partial \boldsymbol{\Sigma}[\boldsymbol{\theta}_0, \mathcal{H}]}{\partial \theta_i} \boldsymbol{\Sigma}^{-1}[\boldsymbol{\theta}_0, \mathcal{H}] \frac{\partial \boldsymbol{\Sigma}[\boldsymbol{\theta}_0, \mathcal{H}]}{\partial \theta_j} \right), \quad (11)$$

where

$$\boldsymbol{\mu}[\boldsymbol{\theta}, \mathcal{H}] \equiv \text{E}[\mathbf{D}] \equiv \int \Pr(\mathbf{D}|\boldsymbol{\theta}, \mathcal{H}) \mathbf{D} d\mathbf{D} \quad (12)$$

and

$$\boldsymbol{\Sigma}[\boldsymbol{\theta}, \mathcal{H}] \equiv \text{E}[(\mathbf{D} - \boldsymbol{\mu}[\boldsymbol{\theta}, \mathcal{H}])(\mathbf{D} - \boldsymbol{\mu}[\boldsymbol{\theta}, \mathcal{H}])^T] \equiv \int \Pr(\mathbf{D}|\boldsymbol{\theta}, \mathcal{H}) (\mathbf{D} - \boldsymbol{\mu}[\boldsymbol{\theta}, \mathcal{H}])(\mathbf{D} - \boldsymbol{\mu}[\boldsymbol{\theta}, \mathcal{H}])^T d\mathbf{D} \quad (13)$$

are evaluated at $\boldsymbol{\theta} = \boldsymbol{\theta}_0$, satisfying

$$\text{E} \left[\frac{\partial}{\partial \theta_i} \Pr(\mathbf{D}|\boldsymbol{\theta}, \mathcal{H}) \right] \Big|_{\boldsymbol{\theta}=\boldsymbol{\theta}_0} = 0. \quad (14)$$

To model an imaging array, we use the results (8) and (9) and set

$$D_i = \langle P^i \rangle, \quad (15)$$

$$\Sigma_{ij} = \text{Cov}[P^i, P^j], \quad (16)$$

where P^i is the output of the i th detector. With this substitution it can be seen that the first term of (11) is proportional to $\tau \Delta \omega$, and therefore proportional to the ratio of integration time to coherence time; whereas the second term is independent of this ratio. For (9) to hold the integration time must be much greater than the coherence time, and hence we can ignore the second term of (11). We see that the covariance of the recovered parameters scales with the reciprocal of the number of coherence times per integration time. As the ratio of integration time to coherence time tends to infinity, the uncertainty in the parameters therefore tends to zero, but in reality, the integration time is limited by practical factors.

Note that although the final result is the same as in previous astronomical applications, the physics is significantly different: the fluctuations and correlations depend on the parameters of the model, whereas in previous work the noise terms have been independent of the parameters. It is clearly possible to add parameter independent noise terms to (9), but since the purpose of this paper is to demonstrate the effect of coherence on imaging arrays, we ignore these additional terms.

4 PARAMETRIZATION OF SOURCES AND DETECTORS

In this paper we perform simulations to investigate the ability of different imaging arrays to extract information from a source. We therefore need suitable parametrizations for both the sources and the detectors.

4.1 Parametrization of sources

The performance of an imaging array will clearly depend on the nature of the sources being observed; there is no universal measure of absolute performance. We can however gain considerable insight by investigating the ability of imaging arrays with different coherence lengths and geometries to determine the parameters of a Gaussian–Schell source (Collett & Wolf 1978):

$$Y_{ij}(\mathbf{r}_1, \mathbf{r}_2) = \frac{I}{\sqrt{2\pi\sigma_s^2}} \exp\left(-\frac{|\mathbf{r}_1 - \mathbf{r}_c|^2 + |\mathbf{r}_2 - \mathbf{r}_c|^2}{4\sigma_s^2} - \frac{|\mathbf{r}_1 - \mathbf{r}_2|^2}{2\sigma_g^2}\right), \quad (17)$$

where $\mathbf{r}_c \equiv (x_c, y_c)$ is the position of the source, I is the total power, σ_s is the geometrical width and σ_g is the coherence length. There are several advantages to using such a source in our simulations. Firstly, it is often a good approximation to the coherence function in the focal plane of a telescope when either a point source or incoherent Gaussian source is present on the sky. Secondly, there is a clear modal interpretation: the natural modes of a Gaussian–Schell source are the Gauss–Hermite modes. Thirdly, there are sufficiently few parameters that the Fisher matrices generated can be easily interpreted. There is no explicit reference to wavelength in the Gaussian–Schell parametrization, but in practise the wavelength dependence is implicit in the coherence length and geometrical size of the source.

In the simulations we use the parameter vector

$$\boldsymbol{\theta} = (x_c, y_c, I, \sigma_s)^T. \quad (18)$$

The coherence length σ_g is not included as a parameter to be recovered: our simulations verified that it is highly degenerate with the intensity, and thus leads to a poorly conditioned Fisher matrix. As the coherence length of the incoming field in the focal plane depends primarily on the telescope optics and is therefore usually known, whereas the intensity of the source is a parameter to be determined, we include the intensity but not the coherence length in our parameter vector.

In Section 5.3, we will consider a slightly more complicated source, namely a pair of identical Gaussian–Schell sources. If the sources are not correlated with each other, the coherence tensors can just be added, hence the overall source coherence tensor has the form

$$Y(\mathbf{r}_1, \mathbf{r}_2) = \frac{I}{\sqrt{2\pi\sigma_s^2}} \exp\left(-\frac{|\mathbf{r}_1 - \mathbf{r}_2|^2}{2\sigma_g^2}\right) \times \left(\exp\left(-\frac{|\mathbf{r}_1 - \mathbf{r}_c - \mathbf{r}_{\text{sep}}/2|^2 + |\mathbf{r}_2 - \mathbf{r}_c - \mathbf{r}_{\text{sep}}/2|^2}{4\sigma_s^2}\right) + \exp\left(-\frac{|\mathbf{r}_1 - \mathbf{r}_c + \mathbf{r}_{\text{sep}}/2|^2 + |\mathbf{r}_2 - \mathbf{r}_c + \mathbf{r}_{\text{sep}}/2|^2}{4\sigma_s^2}\right) \right) \quad (19)$$

where $\mathbf{r}_c \equiv (x_c, y_c)$ is the position of the midpoint between the sources. $\mathbf{r}_{\text{sep}} \equiv (x_{\text{sep}}, y_{\text{sep}})$ is the separation vector between the sources. We define the parameter vector for the double Gaussian–Schell source as

$$\boldsymbol{\theta} = (x_c, y_c, x_{\text{sep}}, y_{\text{sep}}, I, \sigma_s)^T. \quad (20)$$

In order that the posterior is unimodal (and hence that the Gaussian approximation can be applied), we impose the requirement that $x_{\text{sep}} \geq 0$, which removes the inherent transpositional degeneracy of the problem.

4.2 Parameterization of bolometric detectors

In general the coherence tensor of a detector will depend on the details of the physics. For the purpose of this paper however we require a general parametrization that is a reasonable approximation to a typical detector, and that incorporates the most important features. Therefore we consider square pixels of uniform absorbtivity, and with a Gaussian correlation function. Such a model is partially coherent and hence multimode. Thus the detector coherence tensor of the a th detector centred at (x^a, y^a) is given by

$$Z_{ij}^a(\mathbf{r}_1, \mathbf{r}_2) = \Theta(x_1 - (x^a - s/2))\Theta((x^a + s/2) - x_1)\Theta(x_2 - (x^a - s/2))\Theta((x^a + s/2) - x_2) \Theta(y_1 - (y^a - s/2))\Theta((y^a + s/2) - y_1)\Theta(y_2 - (y^a - s/2))\Theta((y^a + s/2) - y_2) \exp\left(-\frac{|\mathbf{r}_1 - \mathbf{r}_2|^2}{2c}\right), \quad (21)$$

where s is the detector size, c is the detector coherence length, $\mathbf{r}_n = (x_n, y_n)$, and $\Theta(x)$ is the Heaviside step function.

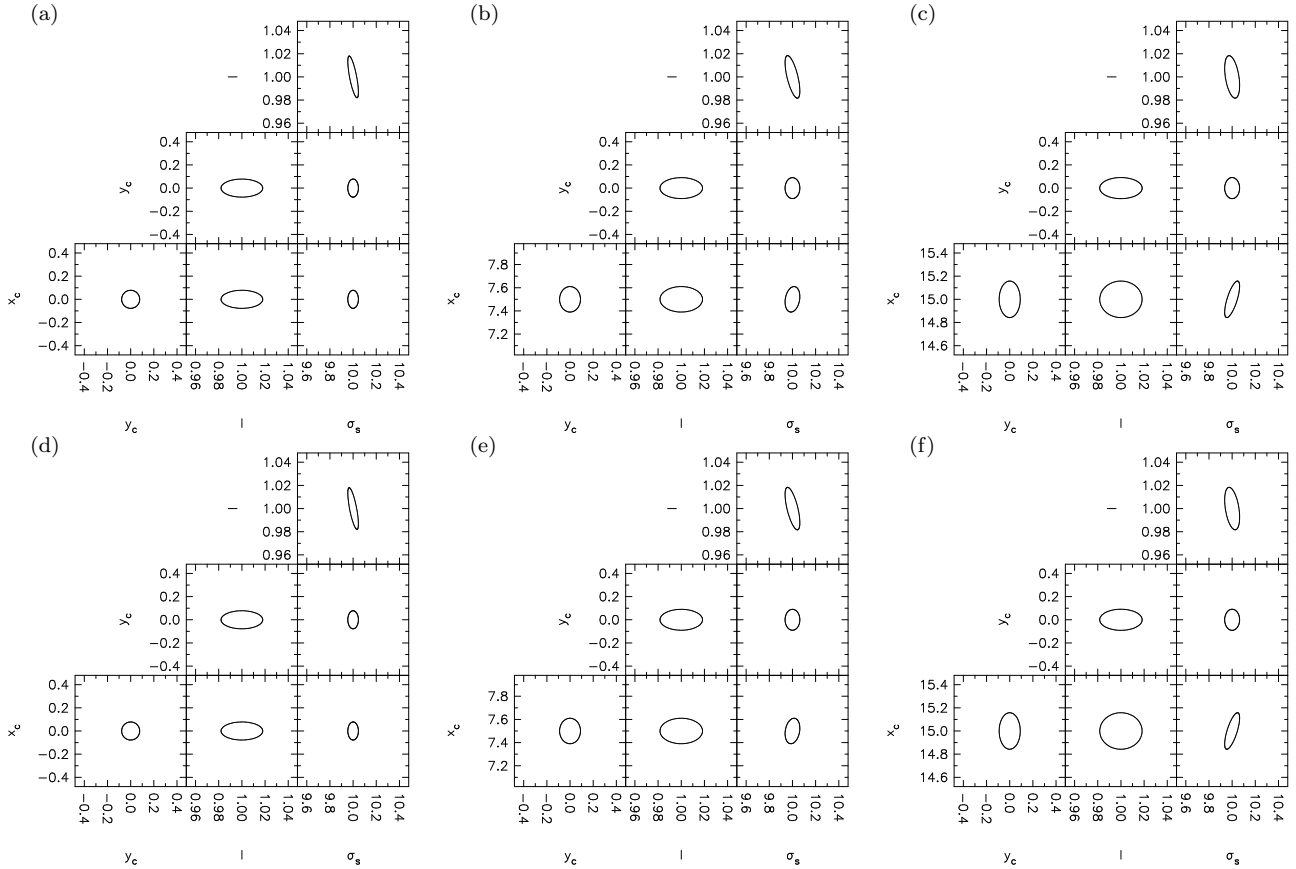


Figure 1. Estimated 80% marginalized confidence contours for the recovered parameters of a Gaussian–Schell source, observed with 5×5 arrays of detectors centered 15 units apart. In all cases the source has parameters $x_c = 0$, $l = 1$, $\sigma_s = 10$ and $\sigma_g = 5$, while the detectors have coherence length $c = 5$, and integration time $\tau = 100/\Delta\omega$. On the top row (a–c), the detector are of side length 15 units, and are thus close packed, while on the bottom row (d–f) they are of side length 3 units, and are therefore sparse. The source is at the centre of the array ($x_c = 0$) in the plots on the left (a, d), while the plots in the middle (c, e) and on the right (d, f) have $x_c = 7.5$ and $x_c = 15$ respectively.

5 SIMULATIONS

We perform all simulations on a uniform 51×51 grid. We use (6) and (7) to perform the discretization, (15), (16), (8) and (9) to calculate the data vector and covariance matrix, and (11) to calculate the Fisher matrix. In the parametrizations for source and detector that follow, we measure all lengths in number of grid points; our results can straightforwardly be scaled to physical units. We set the ratio of integration time to coherence time to be 100. Numerical differencing with a step size of 0.001 was used to calculate the derivatives $\partial D_k/\partial\theta_i$. We verified, by using polynomial interpolation techniques to calculate the derivatives to machine precision in a few random cases, that numerical differencing gives more than sufficient accuracy for the purpose, as well as being much faster. Inversion of the covariance matrix is problematic due to its poor conditioning. To minimise numerical errors and make the inversion stable we therefore employ the pseudo-inverse (Moore 1920; Penrose 1955), discarding singular values below one millionth of the largest singular value. This cut-off is arbitrary, but we found our results were stable through several orders of magnitude of cut-off. Physically, we can justify the use of the pseudo-inverse from the fact that the signal-to-noise ratio falls off rapidly at the edge of the source (Saklatvala, Withington & Hobson 2006), and hence these detectors do not contribute significantly to the Fisher matrix. The effect of taking the pseudo-inverse of the covariance matrix is to discard these same detectors; hence the result is almost identical to that which would be obtained using the true inverse on a machine of unlimited precision.

5.1 Parameter recovery for a Gaussian–Schell source

Figure 1 shows the 80% marginalized confidence contours for the recovered parameters of a Gaussian–Schell source, estimated using the Fisher matrix, when the source is observed with close packed and sparse arrays (see figure caption for details). We observe that all parameters are better constrained with the close packed array, as expected. In all the plots shown, the width of the source is more tightly constrained than its position; this can be predicted from the fact that the source is constrained

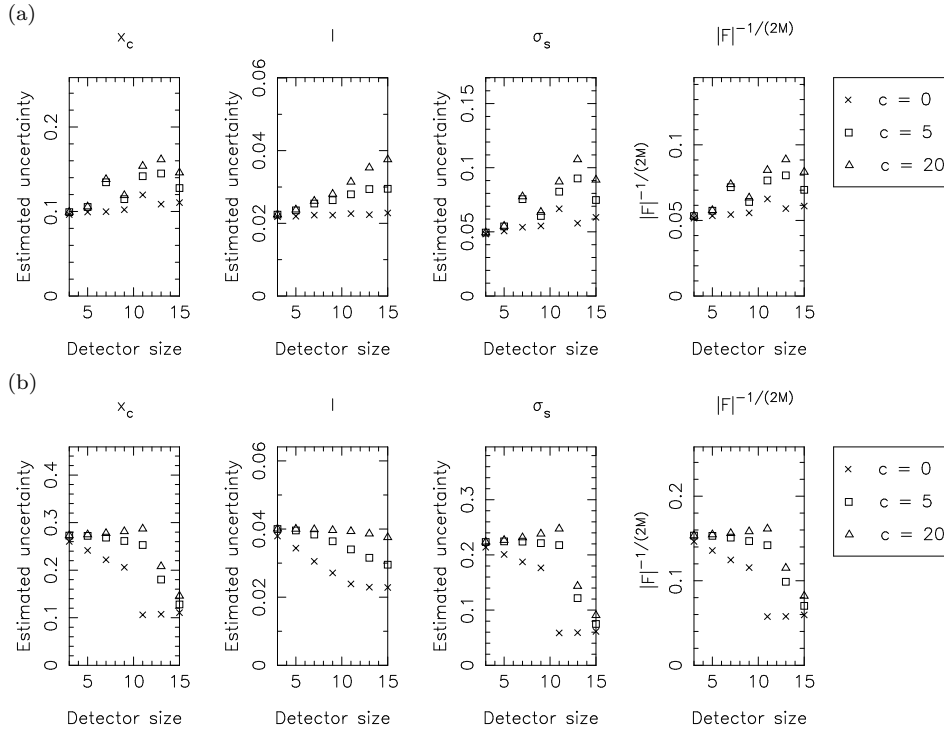


Figure 2. Estimated uncertainties on the recovered parameters (x_c and y_c have the same uncertainties), and the M th root (where M is the number of free parameters in the model, equal to 4), of the estimated allowed volume of parameter space, for a Gaussian–Schell source with parameters $x_c = y_c = 0$, $I = 1$, $\sigma_s = 10$ and $\sigma_g = 5$, observed with arrays of detectors of various size and coherence length (c). In the first row of plots (a), the detectors are close packed, with one detector centered at $(0, 0)$, and a minimum total size of 51×51 units. In the second row (b), the array contains 5×5 detectors centered 15 units apart, such that the array becomes increasingly sparse as the detector size is reduced.

in the model to be circularly symmetric, and thus changing σ_s affects the extent of the source in both x and y directions, and thus affects the output of more detectors than a change in the x or y coordinate alone. When the source is at the centre of the array, the parameters are uncorrelated except the width and intensity, which are anti-correlated. In some of our subsequent simulations the width and intensity are positively correlated. A common theme of this paper is that while our simulations produce all the results that could be straightforwardly predicted, they also uncover many other effects that might not have been expected.

Figure 1 also shows the effect of moving a source away from the centre. We choose the displacements so that the source is centered midway between detectors (centre), and centered on a detector adjacent to the central one (right). We note that there is a minimal difference when the source is centred between detectors, even for the sparse array, where the gaps are 12 units, and thus greater than σ_s . This suggests that as long as neither the gaps between the detectors nor the detector spacing are much larger than σ_s , the position of the source does not affect the amount of information that can be recovered. The implication is that the shoulders of the Gaussian intensity distribution are the important features, not the central peak. Our simulations show on the other hand that losing part of the source off the edge of the array has a dramatic effect on the estimate of the displacement, though less so on the other parameters. It also introduces a correlation between the displacement and the width. When the source is centered on a detector adjacent to the central one, it is centered roughly $1\sigma_s$ from the edge of the array, and these effects are seen clearly.

5.2 Effect of detector size and coherence on close-packed and sparse arrays

We have seen that sparse arrays of small detectors are less effective at recovering source parameters than close packed arrays of large detectors, but now we investigate in detail the effects of both detector size and coherence, and distinguish between the effect of detector size and the effect of the number of detectors in the array.

Figure 2 shows the estimated uncertainty on the recovered parameters of the same Gaussian–Schell source as in Section 5.1, with close packed and sparse arrays of detectors of various size and coherence (see figure caption for details). We also show the quantity $|F|^{-1/(2M)}$, where F is the Fisher matrix and M is the number of parameters in the model. This quantity can be interpreted as the M th root of the estimated allowed volume of parameter space, and gives a measure of the overall

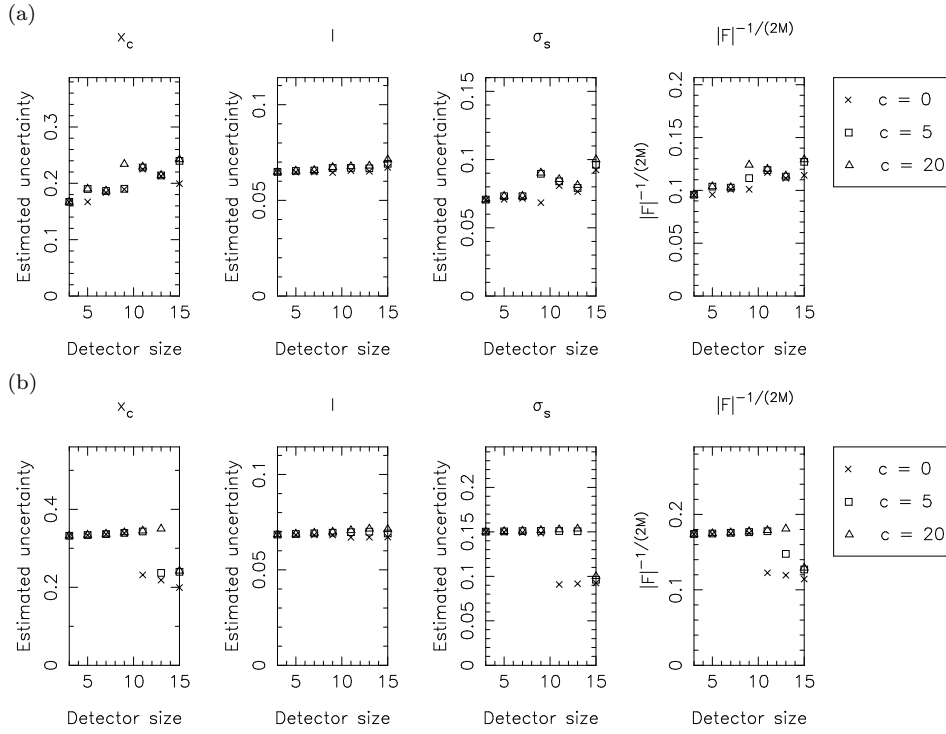


Figure 3. Estimated uncertainties on the recovered parameters, and the M th root of the estimated allowed volume of parameter space, for a Gaussian–Schell source observed with close packed and sparse arrays of detectors of various size and coherence length. The sources and arrays are identical to those in Figure 2, except that the coherence length of the source is increased such that $\sigma_g = 20$.

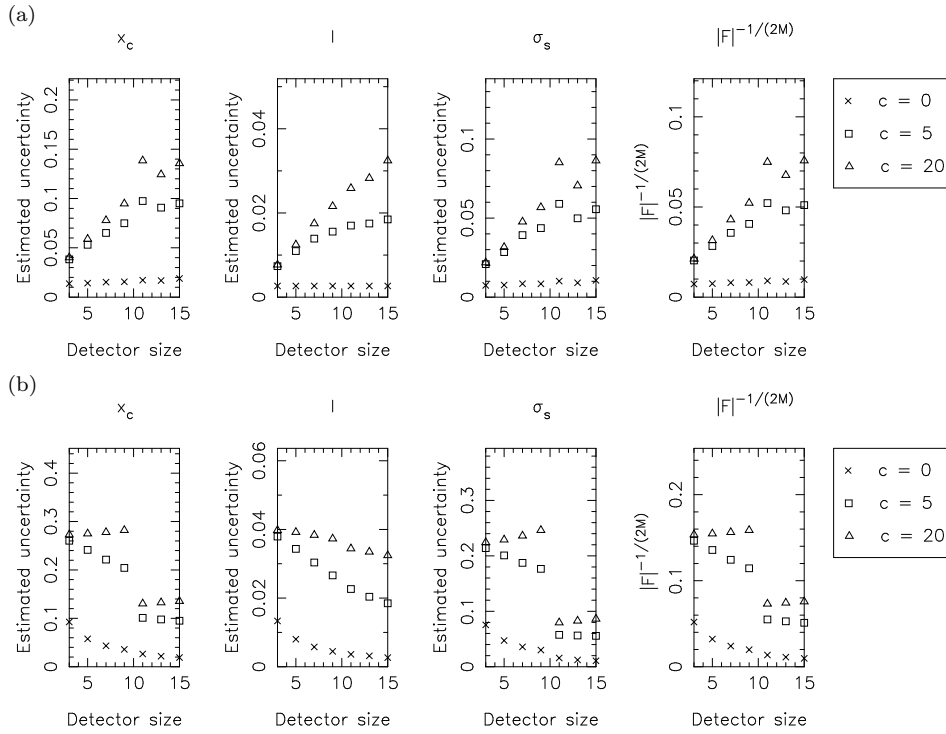


Figure 4. Estimated uncertainties on the recovered parameters, and the M th root of the estimated allowed volume of parameter space, for a Gaussian–Schell source observed with close packed and sparse arrays of detectors of various size and coherence length. The sources and arrays are identical to those in Figure 2, except that the source is incoherent ($\sigma_g = 0$).

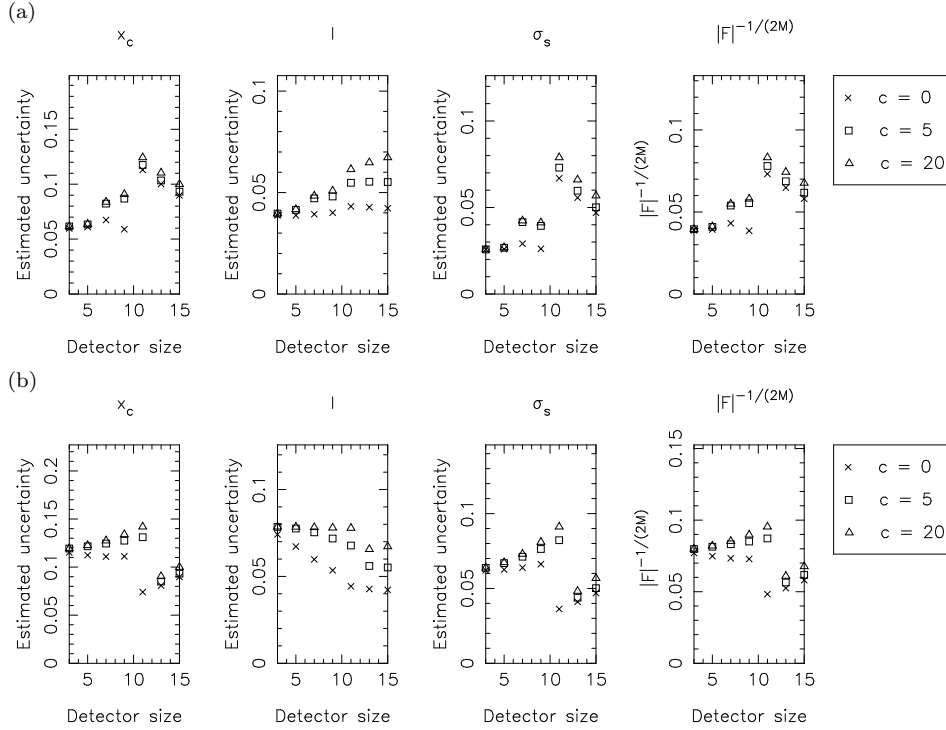


Figure 5. Estimated uncertainties on the recovered parameters, and the M th root of the estimated allowed volume of parameter space, for a Gaussian–Schell source observed with close packed and sparse arrays of detectors of various size and coherence length. The sources and arrays are identical to those in Figure 2, except that the geometric size of the source is reduced such that $\sigma_s = 5$.

uncertainty in the measurement. If the parameters are uncorrelated, it will be equal to the geometric mean of the uncertainties on the individual parameters, but if they are correlated it will be less.

We can identify many trends. The more coherent the detector the less accurately the source parameters can be determined, as would be expected from our detector model, in which more coherent detectors have inferior signal to noise. Furthermore, this effect becomes more significant as the detector size increases; again this is to be expected, as the coherence makes little difference to a small detector. A final general comment is that the uncertainty in the intensity follows smooth trends for both close packed and sparse arrays, while the behaviour of the position parameters, which is more complicated, is always the same as that of the width.

For the close packed arrays, the uncertainty of the parameter estimates generally increases with detector size. However, the detailed behaviour is much more complicated. The incoherent detectors give almost identical accuracy regardless of the size. The uncertainty on the intensity increases progressively with detector size whereas the uncertainties on the position and width rises and falls twice, but with an underlying increasing trend. The tendency to less accurate parameter recovery with increasing size can be attributed only in part to reduced spatial resolution, as the effect is much less for incoherent detectors. Rather the trends seen appear to be caused by the details of the coupling of the natural modes of the detector to the natural modes of the source.

In the case of the sparse arrays with fixed number of pixels, we find in all cases that the uncertainty in the intensity falls gradually as the detector size increases, while there is a step change in the other parameters at a size of around 11 units. The detailed behaviour depends on the coherence length; for the coherent detectors, the uncertainty actually *increases* with size up to a threshold, then falls, whereas for the less coherent detectors the uncertainty falls gradually up to the threshold, then suddenly, before plateauing. Furthermore, the precise threshold size depends on the coherence length.

We now investigate how the size and coherence length of the source changes our results. Figure 3 shows the same information as Figure 2, except that the coherence length of the source is increased fourfold. We see a number of changes in the behaviour. The effect of the coherence of the detector is now generally much less pronounced. The uncertainty on the intensity is almost independent of detector size. The uncertainty on the position and width for the close packed arrays show the same complicated behaviour as before, but the peaks are shifted. For the sparse arrays, we still see the step change at around 11 units, but almost no variation below that threshold. The coherence length of the detector does affect the position of this transition, hence when the size is around 11 units the detector coherence length *does* make a significant difference. Finally we see that the uncertainties on all parameters are greater than for the less coherent source, as expected, because the signal to noise is worse.

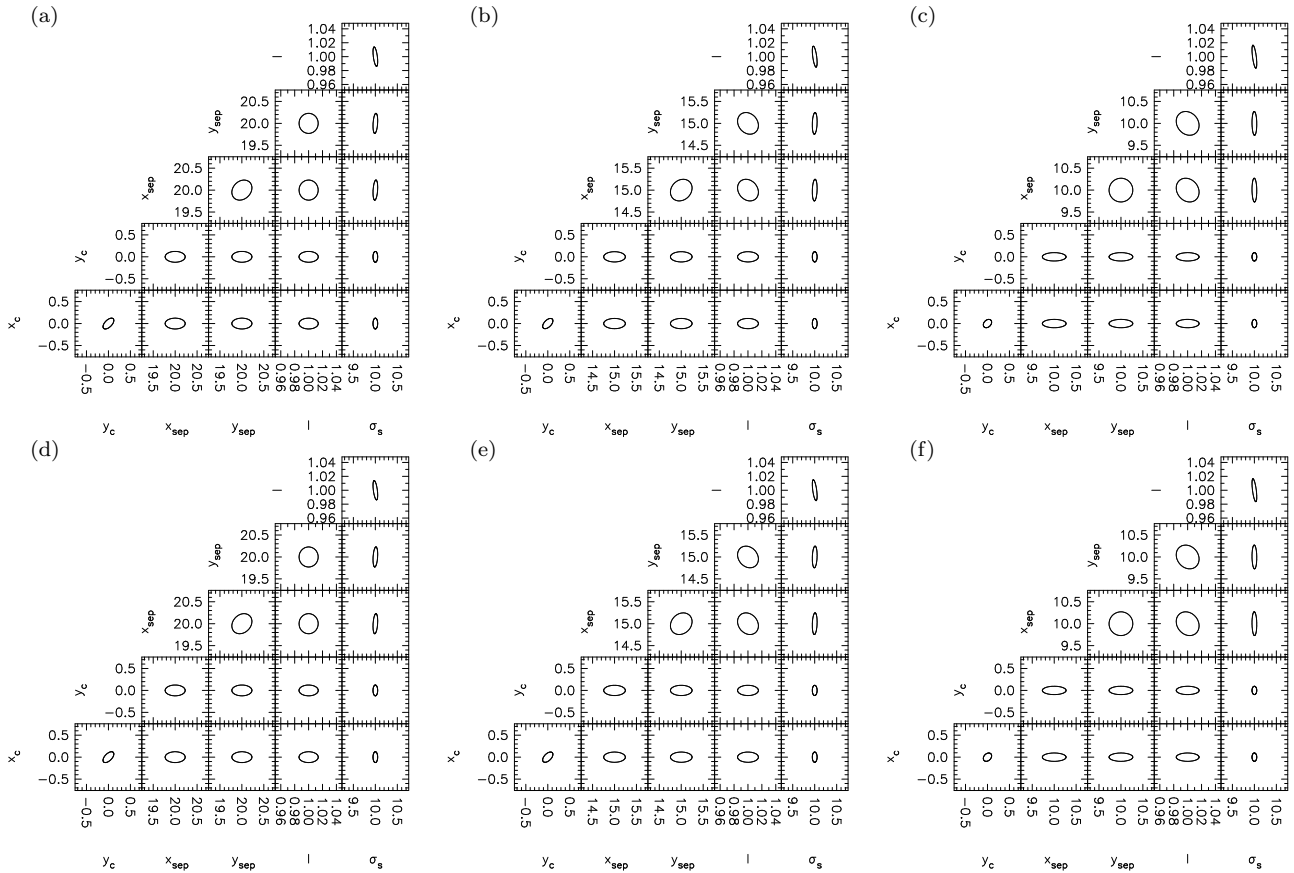


Figure 6. Estimated 80% marginalized confidence contours for the recovered parameters of a pair of identical Gaussian–Schell sources, observed with 5×5 arrays of detectors centered 15 units apart. In all cases the source has parameters $x_c = y_c = 0$, $y_{sep} = 0$, $I = 1$, $\sigma_s = 10$ and $\sigma_g = 5$, while the detectors have coherence length $c = 5$. On the top row (a–c), the detector are of side 15 units, and are thus close packed, while on the bottom row (d–f) they are of side 3 units, and are therefore sparse. The sources are separated in both the x and y directions with $x_{sep} = y_{sep} = 10$ (a, d), $x_{sep} = y_{sep} = 15$ (b, e) and $x_{sep} = y_{sep} = 20$ (c, f).

Figure 4 shows the same information as Figure 2, except that the source is incoherent. The opposite effects are seen as in Figure 3: the detector coherence length is much more important, the step change for the sparse arrays is still present, though less obviously for the incoherent detector, whereas the other trends are more pronounced. The peaks and troughs for the position and uncertainty with the close packed arrays are shifted yet again, though not predictably. The uncertainties on all parameters are less than for the partially coherent sources, as expected.

Figure 5 shows the same information as Figure 2, except that the size of the source is halved. Most of the trends are very similar, but the obvious difference is the sharp peak in the uncertainty of the position and width estimates for the close packed array with size 11 units. There is also some slight discrepancy in behaviour between the position and width estimates, which was not seen in Figure 2. More telling however is the fact that the step change for the sparse arrays is not shifted either by changing the size or coherence of the source. It is not therefore simply caused by matching the size of the detectors to either size or coherence length of the source; rather the most important factor seems to be the fraction of the focal plane covered by the detectors. Finally, the errors on the position and size are less than in Figure 2, though the error on the intensity is greater.

In this section, we have seen that apart from a few predictable trends, most of the behaviour of imaging arrays is quite complicated and not possible to predict by straightforward physical arguments. The complexity appears to be due to the details of how the natural modes of the source (in this case the Gauss–Hermite modes) couple to the modes of the detectors. Indeed, when the length scales of source and detectors are similar, and the sources and detectors are partially coherent, there is no reason to expect simple behaviour. Our simulations have demonstrated the importance of performing detailed simulations whenever partially coherent arrays are to be designed. Nevertheless, there are a number of key trends to emerge. Firstly the coherence of both detector and source have a significant effect on the parameter recovery. Secondly, the packing density needs to be above a certain threshold for information to be recovered. This packing density is roughly independent of the source parameters, and corresponds to roughly 50% of the focal plane being filled.

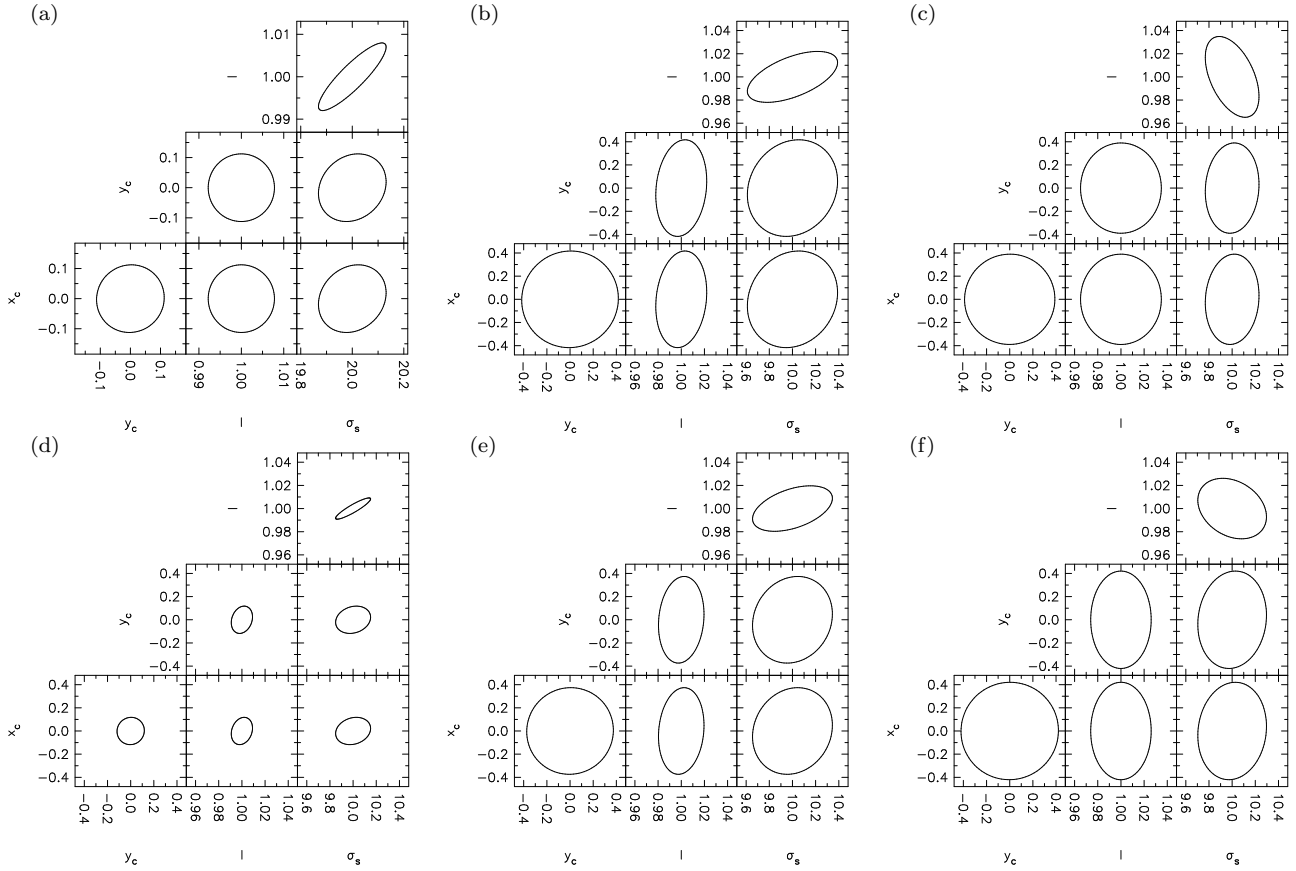


Figure 7. Estimated 80% marginalized confidence contours for the recovered parameters of a Gaussian–Schell source, observed with 17×17 close packed arrays of detectors of size 3 units and coherence 10 units, but with only 8×8 channels, so each channel is attached to 4 detectors. In the top row (a–c), 2×2 clusters of adjacent detectors are joined to the same channel, while in the bottom row (d–f) the detectors on each channel are interlaced, such that there is one interposing detector between detectors on the same channel. In all cases the source has parameters $x_c = 0$, $I = 1$, $\sigma_s = 20$. The source has coherence length $\sigma_g = 0$ (a, d), $\sigma_g = 10$ (b, e) and $\sigma_g = 30$ (c, f).

5.3 Parameter recovery for a double Gaussian–Schell source

We now consider a slightly more complicated source: the double Gaussian–Schell source defined by (19). Figure 6 shows the 80% confidence contours of the parameters of such sources with various separation vectors, when observed with both close–packed and sparse arrays. As the sources are moved apart in the x direction, x_c becomes better constrained, but the other parameters become less well constrained, due to part of the source moving off the edge of the array. The same effect is seen for both close packed and sparse arrays. The source parameters can be equally well inferred even when the sources are strongly overlapping. However, this is not to say that the sources can be resolved: in order to determine whether two sources are resolved, it is necessary to compare models, for instance a pair of identical circularly symmetric sources with a single elliptical source. Fisher matrix analysis is not sufficient for this purpose; however, our coupled mode theory of detectors allows the higher moments, and hence the full likelihood function of the detector outputs to be calculated, and thus, in principle, it enables a detailed Bayesian analysis to be carried out. For the purpose of this paper, we simply consider Figure 6 to be a demonstration of how the Fisher matrix technique can be applied to complex sources of known form.

5.4 Reduced channel arrays: effect of interlacing detectors on the different channels

In a real imaging array, there is a multiplexing problem, and so it is often desirable to make the number of channels smaller than the number of detectors, by connecting multiple detectors to the same channel, such that the output of the channel is the sum of the outputs of the individual detectors. The question then arises: given a certain number of detectors and a certain number of channels, what is the best way to group the detectors feeding into each channel? The most obvious configuration is to have contiguous blocks of detectors on the same channel, but the complexity of behaviour we have seen in our previous simulations suggests that in some circumstances, it may be desirable to interlace the detectors on the different channels.

We consider a close packed 17×17 array of detectors of size 3 units and coherence length 10 units, but with 4 detectors attached to each channel. In the top row of Figure 7 we show the recovered parameters of sources of different coherence

lengths where the 4 detectors on each channel form a 2×2 contiguous block. In the bottom row, the detectors on the different channels are interlaced such that the 4 detectors on each channel are at the corners of a 3×3 block.

For the incoherent source, all the parameters are less well constrained for the interlaced channels than the contiguous ones; for the partially coherent source ($\sigma_g = 10$), the parameters are better constrained for the interlaced channels, and for the fully coherent source ($\sigma_g = 30$), the position and width are worse constrained, but the intensity is better constrained, for the interlaced array. The effects are quite small because the arrays remain close packed, and the “effective pixel size” varies only from 6 to 9 units; Figures 2 to 5 would suggest a relatively small effect over this range. However, it is possible that with many detectors on each channel, and with the detectors on each channel spread over a wider area, these effects may be amplified. The complexity introduced makes further exploration beyond the scope of this paper; however it is a potentially important area for future work.

6 CONCLUSION

We have combined our coupled-mode theory of detection with Fisher information techniques from signal processing to study the performance of imaging arrays. Several of our results have important implications for array design. We have found that there is a threshold packing density above which the detectors must be packed for information to be recovered, and that this threshold has little dependence on the size and coherence of the source. Above and below this threshold, the packing density makes relatively little difference. As long as the source is not much smaller than the detector spacing, the same information can be obtained regardless of its position, even for sparse arrays. On the other hand, the coherence length of both source and detectors makes a significant difference to the amount of information that can be obtained. Most importantly of all, we have shown that detailed simulations are necessary for understanding the behaviour of imaging arrays. The reason for this is that the behaviour results from the coupling between the natural modes of the array and the natural modes of the source; when the source and detectors are multimode, the behaviour thus becomes too complicated to be explained by straightforward physical arguments.

Numerous extensions to our work are possible. One could study the effects of photon occupancy for instance, or use a more sophisticated model for the detectors. One could consider more complicated array geometries, and explore the issue of interlaced pixels in more detail: our results in this paper are inconclusive, but enough to suggest that interlaced pixels may be preferable in certain conditions. Perhaps most interestingly, one could investigate whether putting the outputs of the detectors through a correlator enables more information to be recovered, and can be used to mitigate the poor signal to noise ratios for detectors placed in highly coherent fields.

APPENDIX A: ALTERNATIVE DEFINITION OF THE FISHER MATRIX

The definition of the Fisher matrix in (10) is that used by most astronomers; however there is an equivalent definition (Kendall & Stuart 1967), that is necessary to derive the Cramér–Rao bound. Define the score vector $\mathbf{V}[\boldsymbol{\theta}, \mathcal{H}]$ by

$$V_i[\boldsymbol{\theta}, \mathcal{H}] \equiv \frac{\partial}{\partial \theta_i} \ln \Pr(\mathbf{D}|\boldsymbol{\theta}, \mathcal{H}) . \quad (\text{A1})$$

We now show that the Fisher matrix is equivalent to the covariance of the score. From the definition of the score in (A1) we can show trivially that

$$E[V_i] = 0 , \quad (\text{A2})$$

and therefore the covariance is given by

$$\begin{aligned} \text{Cov}[V_i[\boldsymbol{\theta}, \mathcal{H}], V_j[\boldsymbol{\theta}, \mathcal{H}]] &= E \left[\frac{\partial \ln \Pr(\mathbf{D}|\boldsymbol{\theta}, \mathcal{H})}{\partial \theta_i} \frac{\partial \ln \Pr(\mathbf{D}|\boldsymbol{\theta}, \mathcal{H})}{\partial \theta_j} \right] \\ &= \int \Pr(\mathbf{D}|\boldsymbol{\theta}, \mathcal{H}) \frac{\partial \ln \Pr(\mathbf{D}|\boldsymbol{\theta}, \mathcal{H})}{\partial \theta_i} \frac{\partial \ln \Pr(\mathbf{D}|\boldsymbol{\theta}, \mathcal{H})}{\partial \theta_j} d\mathbf{D} \\ &= \int \frac{1}{\Pr(\mathbf{D}|\boldsymbol{\theta}, \mathcal{H})} \frac{\partial \Pr(\mathbf{D}|\boldsymbol{\theta}, \mathcal{H})}{\partial \theta_i} \frac{\partial \Pr(\mathbf{D}|\boldsymbol{\theta}, \mathcal{H})}{\partial \theta_j} d\mathbf{D} . \end{aligned} \quad (\text{A3})$$

The Fisher matrix, as defined in (10), is given by

$$\begin{aligned} F_{ij}[\boldsymbol{\theta}, \mathcal{H}] &= - \int \Pr(\mathbf{D}|\boldsymbol{\theta}, \mathcal{H}) \frac{\partial^2 \ln \Pr(\mathbf{D}|\boldsymbol{\theta}, \mathcal{H})}{\partial \theta_i \partial \theta_j} d\mathbf{D} \\ &= - \int \frac{\partial^2 \Pr(\mathbf{D}|\boldsymbol{\theta}, \mathcal{H})}{\partial \theta_i \partial \theta_j} d\mathbf{D} + \int \frac{1}{\Pr(\mathbf{D}|\boldsymbol{\theta}, \mathcal{H})} \frac{\partial \Pr(\mathbf{D}|\boldsymbol{\theta}, \mathcal{H})}{\partial \theta_i} \frac{\partial \Pr(\mathbf{D}|\boldsymbol{\theta}, \mathcal{H})}{\partial \theta_j} d\mathbf{D} . \end{aligned} \quad (\text{A4})$$

But

$$\int \frac{\partial^2 \Pr(\mathbf{D}|\boldsymbol{\theta}, \mathcal{H})}{\partial \theta_i \partial \theta_j} d\mathbf{D} = \frac{\partial^2}{\partial \theta_i \partial \theta_j} \int \Pr(\mathbf{D}|\boldsymbol{\theta}, \mathcal{H}) d\mathbf{D} = 0, \quad (\text{A5})$$

so by comparing (A4) with (A3) we find that

$$F_{ij}[\boldsymbol{\theta}, \mathcal{H}] = \text{Cov}[V_i[\boldsymbol{\theta}, \mathcal{H}], V_j[\boldsymbol{\theta}, \mathcal{H}]], \quad (\text{A6})$$

which is the alternative definition of the Fisher matrix.

APPENDIX B: DERIVATION OF THE MULTI-PARAMETER CRAMÉR-RAO BOUND

Consider a statistic vector $\mathbf{T} = \mathbf{t}(\mathbf{D})$, that is an unbiased estimator of the parameter vector $\boldsymbol{\theta}$, i.e.

$$\mathbb{E}[\mathbf{T}] = \boldsymbol{\theta}. \quad (\text{B1})$$

Let \mathbf{C} be the covariance matrix of the estimators:

$$\mathbf{C} \equiv \mathbb{E}[(\mathbf{T} - \boldsymbol{\theta})(\mathbf{T} - \boldsymbol{\theta})^T] \quad (\text{B2})$$

Now, using the definition of the score in (A1), we have

$$\begin{aligned} \mathbb{E}[V_i T_j] &= \int T_j \frac{\partial}{\partial \theta_i} \Pr(\mathbf{D}|\boldsymbol{\theta}) d\mathbf{D} \\ &= \frac{\partial}{\partial \theta_i} \mathbb{E}[T_j] \\ &= \delta_{ij}. \end{aligned} \quad (\text{B3})$$

Now form the matrix $\mathbb{E}[(\mathbf{T} - \boldsymbol{\theta} - \mathbf{W}\mathbf{V})(\mathbf{T} - \boldsymbol{\theta} - \mathbf{W}\mathbf{V})^T]$, where \mathbf{W} is some arbitrary matrix. By forming a quadratic form with some arbitrary vector \mathbf{x} , it is clear that

$$\mathbb{E}[(\mathbf{T} - \boldsymbol{\theta} - \mathbf{W}\mathbf{V})(\mathbf{T} - \boldsymbol{\theta} - \mathbf{W}\mathbf{V})^T] \geq \mathbf{0}, \quad (\text{B4})$$

i.e. the matrix on the left of the inequality is positive semi-definite. Expanding the left hand side of (B4), using (A6), (A2) and (B3), and rearranging, we obtain

$$\mathbf{C} \geq \mathbf{W} + \mathbf{W}^T - \mathbf{W}\mathbf{F}\mathbf{W}^T. \quad (\text{B5})$$

Each matrix \mathbf{W} gives us a different lower bound: to find the maximum lower bound we diagonalize the Fisher matrix $\mathbf{F} = \mathbf{Q}\boldsymbol{\Lambda}\mathbf{Q}^T$. It can then be easily shown that

$$\mathbf{W} + \mathbf{W}^T - \mathbf{W}\mathbf{F}\mathbf{W}^T = \mathbf{Q}\boldsymbol{\Lambda}\mathbf{Q}^T - (\mathbf{W}\mathbf{Q} - \mathbf{Q}\boldsymbol{\Lambda}^{-1})\boldsymbol{\Lambda}(\mathbf{W}\mathbf{Q} - \mathbf{Q}\boldsymbol{\Lambda}^{-1})^T. \quad (\text{B6})$$

Hence the maximum lower bound is obtained for $\mathbf{W} = \mathbf{F}^{-1}$. Substituting back in (B5) we obtain

$$\mathbf{C} \geq \mathbf{F}^{-1}. \quad (\text{B7})$$

APPENDIX C: FISHER MATRIX FOR GAUSSIAN LIKELIHOOD

The Gaussian approximation to the likelihood function is

$$\Pr(\mathbf{D}|\boldsymbol{\theta}, \mathcal{H}) = \frac{1}{(2\pi)^{M/2} |\boldsymbol{\Sigma}[\boldsymbol{\theta}, \mathcal{H}]|^{1/2}} \exp\left(-\frac{1}{2}(\mathbf{D} - \boldsymbol{\mu}[\boldsymbol{\theta}, \mathcal{H}])^T \boldsymbol{\Sigma}^{-1}[\boldsymbol{\theta}, \mathcal{H}] (\mathbf{D} - \boldsymbol{\mu}[\boldsymbol{\theta}, \mathcal{H}])\right), \quad (\text{C1})$$

where M is the number of parameters in the model. Henceforth, for brevity, we do not show the dependence of $\boldsymbol{\mu}$ and $\boldsymbol{\Sigma}$ on the model and its parameters explicitly in our notation. We can thus write

$$\ln \Pr(\mathbf{D}|\boldsymbol{\theta}, \mathcal{H}) = -\frac{1}{2}(\mathbf{D} - \boldsymbol{\mu})^T \boldsymbol{\Sigma}^{-1}(\mathbf{D} - \boldsymbol{\mu}) - N/2 \ln(2\pi) - \frac{1}{2} \ln |\boldsymbol{\Sigma}|, \quad (\text{C2})$$

$$\frac{\partial \ln \Pr(\mathbf{D}|\boldsymbol{\theta}, \mathcal{H})}{\partial \theta_i} = \frac{\partial \boldsymbol{\mu}^T}{\partial \theta_i} \boldsymbol{\Sigma}^{-1}(\mathbf{D} - \boldsymbol{\mu}) - \frac{1}{2} \frac{\partial \ln |\boldsymbol{\Sigma}|}{\partial \theta_i} - \frac{1}{2} (\mathbf{D} - \boldsymbol{\mu})^T \frac{\partial \boldsymbol{\Sigma}^{-1}}{\partial \theta_j} (\mathbf{D} - \boldsymbol{\mu}) \quad (\text{C3})$$

From (10) the Fisher matrix is given by

$$\begin{aligned} F_{ij}[\boldsymbol{\theta}, \mathcal{H}] &= -\mathbb{E}\left[\frac{\partial^2 \ln \Pr(\mathbf{D}|\boldsymbol{\theta}, \mathcal{H})}{\partial \theta_i \partial \theta_j}\right] \\ &= \frac{\partial \boldsymbol{\mu}^T}{\partial \theta_i} \boldsymbol{\Sigma}^{-1} \frac{\partial \boldsymbol{\mu}}{\partial \theta_j} + \frac{1}{2} \frac{\partial^2 \ln |\boldsymbol{\Sigma}|}{\partial \theta_i \partial \theta_j} + \frac{1}{2} \text{Tr}\left(\boldsymbol{\Sigma} \frac{\partial^2 \boldsymbol{\Sigma}^{-1}}{\partial \theta_i \partial \theta_j}\right) \end{aligned} \quad (\text{C4})$$

For the parameter values that maximize the likelihood, we set the expectation of the first derivative equal to zero, to obtain

$$\frac{\partial \ln |\Sigma|}{\partial \theta_i} = -\text{Tr} \left(\Sigma \frac{\partial \Sigma^{-1}}{\partial \theta_i} \right) \quad (\text{C5})$$

and thus

$$F_{ij}[\boldsymbol{\theta}, \mathcal{H}] = \frac{\partial \boldsymbol{\mu}^T}{\partial \theta_i} \Sigma^{-1} \frac{\partial \boldsymbol{\mu}}{\partial \theta_j} - \text{Tr} \left(\frac{\partial \Sigma}{\partial \theta_j} \frac{\partial \Sigma^{-1}}{\partial \theta_i} \right). \quad (\text{C6})$$

Finally we can write

$$\begin{aligned} \text{Tr} \left(\frac{\partial \Sigma}{\partial \theta_j} \frac{\partial \Sigma^{-1}}{\partial \theta_i} \right) &= \text{Tr} \left(\frac{\partial \Sigma}{\partial \theta_j} \frac{\partial (\Sigma^{-1} \Sigma \Sigma^{-1})}{\partial \theta_i} \right) \\ &= 2\text{Tr} \left(\frac{\partial \Sigma}{\partial \theta_j} \frac{\partial \Sigma^{-1}}{\partial \theta_i} \right) + \text{Tr} \left(\Sigma^{-1} \frac{\partial \Sigma}{\partial \theta_i} \Sigma^{-1} \frac{\partial \Sigma}{\partial \theta_j} \right) \\ &= -\text{Tr} \left(\Sigma^{-1} \frac{\partial \Sigma}{\partial \theta_i} \Sigma^{-1} \frac{\partial \Sigma}{\partial \theta_j} \right), \end{aligned} \quad (\text{C7})$$

and thus we obtain (11).

REFERENCES

- Abramovich Y. I., Gray D. A., Spencer N. K., Gorokhov A. Y., 1996, Proc. EUSIPCO, 2, 915
 Adorf H.-M., 1996, ASP Conf. Ser., 101, 13
 Collett E., Wolf E., 1978, Opt. Lett., 2, 27
 Dicke R. H., 1946, Rev. Sci. Instrum., 177, 268
 Dicker S. R., Abrahams J., Ade P. A. R., Ames T. J., Benford D. J., Chen T. C., Chervenak J. A., Devlin M. J., Irwin K. D., Korngut P. M., Maher S., Mason B. S., Mello M., Moseley S. H., Norrod R. D., Shafer R. A., Staguhn J. G., Talley D. J., Tucker C., Werner B. A., White S. D., 2006, Proc. SPIE, 6275, 62751B
 Dowell C. D., Allen C. A., Babu R. S., Freund M. M., Gardner M., Groseth J., Jhabvala M. D., Kovacs A., Lis D. C., Moseley S. H., Phillips T. G., Silverberg R. F., Voellmer G. M., Yoshida H., 2003, Proc. SPIE, 4855, 73
 Evans R., Harper D. A., Casey S., Davidson J. A., Gatley I., Kastner J., Loewenstein R., Moseley S. H., Pernic R., Wirth J., 2002, EAS Pub. Ser., 4, 239
 Fowler J. W., 2004, Proc. SPIE, 5498, 1
 Hamilton A. J. S., 1997, MNRAS, 289, 285
 Hanbury Brown R., Twiss R. Q., 1956, Nat, 177, 27
 Holland W., MacIntosh M., Fairley A., Kelly D., Montgomery D., Gostick D., Atad-Ettedgui E., Ellis M., Robson I., Hollister M., Woodcraft A., Ade P., Walker I., Irwin K., Hilton G., Duncan W., Reintsema C., Walton A., Parkes W., Dunare C., Fich M., Kycia J., Halpern M., Scott D., Gibb A., Molnar J., Chapin E., Bintley D., Craig S., Chylek T., Jenness T., Economou F., Davis G., 2006, Proc. SPIE, 6275, 62751E
 Kendall M. G., Stuart A., 1967, The Advanced Theory of Statistics. Hafner Publishing, New York
 Maffei B., Ade P. A. R., Calderon C., Challinor A. D., Bernardis P. D., Dunlop L., Gear W. K., Giraud-Héraud Y., Goldie D. J., Grainge K. J. B., Isaak K. G., Johnson B., Jones M. E., Lasenby A. H., Mauskopf P. D., Melhuish S. J., Orlando A., Piccirillo L., Pisano G., Taylor A. C., Withington S., Yassin G., 2005, EAS Pub. Ser., 14, 251
 Martins C. J., Melchiorri A., Bean R., Rocha G., Avelino P. P., Viana P. T., 2002, Phys. Rev. D, 66
 Marzetta T. L., 1993, IEEE Trans. Signal Processing, 41, 2247
 Moore E. H., 1920, Bull. Am. Math. Soc., 26, 394
 Penrose R., 1955, Proc. Cambridge Phil. Soc., 51, 406
 Rocha G., Trotta R., Martins C. J. A. P., Melchiorri A., P. P. A., Bean R., Viana P. T. P., 2004, MNRAS, 352, 20
 Saklatvala G., Withington S., Hobson M. P., 2006, Proc. SPIE, 6275, 62750R
 Saklatvala G., Withington S., Hobson M. P., 2007, J. Opt. Soc. Am. A, 24, in press
 Staguhn J. G., Benford D. J., Allen C. A., Moseley S. H., Sharp E. H., Ames T. J., Brunswig W., Chuss D. T., Dwek E., Maher S. F., Marx C. T., Miller T. M., Navarro S., Wollack E. J., 2006, Proc. SPIE, 6275, 62751D
 Stoica P., Nehorai A., 1989, IEEE Trans. Acoust. Speech Signal Processing, 37, 720
 Tegmark M., Taylor A. N., Heavens A. F., 1997, ApJ, 480, 22
 Withington S., Hobson M. P., Saklatvala G., 2005, J. Opt. Soc. Am., 22, 1937
 Withington S., Yassin G., 2001, J. Opt. Soc. Am., 18, 3061
 Withington S., Yassin G., 2002, J. Opt. Soc. Am., 19, 1376

Yamamoto K., Kadoya Y., Murata T., Futamase T., 2001, *Prog. Theor. Phys.*, 106, 917
Zmuidzinis J., 2003, *Appl. Opt.*, 42, 4989